

# From Single-Point to Multi-Point Reflection Modeling: Robust Vital Signs Monitoring via mmWave Sensing

Duo Zhang<sup>ID</sup>, Xusheng Zhang<sup>ID</sup>, Yaxiong Xie<sup>ID</sup>, Fusang Zhang<sup>ID</sup>, Hongliu Yang<sup>ID</sup>, and Daqing Zhang<sup>ID</sup>, *Fellow, IEEE*

**Abstract**—Long-term monitoring of human vital signs like respiration and heartbeat is crucial for the early detection of diverse diseases and overall health monitoring. Contact-free vital signs monitoring using wireless signals, particularly mmWave-based methods, has gained attention due to its sensitivity and privacy-preserving benefits. However, we observe that even minor human movements could lead to significant mutations in the signal-to-noise ratio (SNR) of the wireless signal, which cannot be explained by the commonly used model that represents the human chest as a single reflection point. These fluctuations challenge the robustness of heart rate and heart rate variability (HRV) monitoring due to the vulnerability of faint heartbeats to noise interference. To tackle this, we introduce a multi-point reflection model to understand the underlying causes of SNR fluctuations and propose a frequency diversity based algorithm to enhance sensing SNR. Our solution, Robust-Vital, was rigorously evaluated using commercial mmWave radar systems and demonstrated superior performance on long-term heart rate and heart rate variability tracking in a user study with 12 participants.

**Index Terms**—MmWave radar, multi-reflection model, robustness, vital signs, wireless sensing.

## I. INTRODUCTION

CONTINUOUSLY and daily tracking of vital signs like respiration and heartbeat is critical for early detection of

Received 23 January 2024; revised 21 June 2024; accepted 20 August 2024. Date of publication 26 August 2024; date of current version 5 November 2024. This work was supported by NSFC A3 Foresight Program under Grant 62061146001. Recommended for acceptance by M. Pierobon. (*Corresponding author: Daqing Zhang*.)

This work involved human subjects or animals in its research. Approval of all ethical and experimental procedures and protocols was granted by Committee of Peking University First Hospital under Application No. 2021297, and performed in line with the Declaration of Helsinki.

Duo Zhang, Xusheng Zhang, and Hongliu Yang are with the Key Lab of High Confidence Software Technologies (Ministry of Education), School of Computer Science, Peking University, Beijing 100871, China (e-mail: zhangduo@stu.pku.edu.cn; zhangxusheng@stu.pku.edu.cn; Hongliu\_yang@stu.pku.edu.cn).

Yaxiong Xie is with the University at Buffalo, Buffalo, NY 14203 USA (e-mail: yaxiongx@buffalo.edu).

Fusang Zhang is with the Institute of Software, Chinese Academy of Sciences, University of Chinese Academy of Sciences, Beijing 100190, China (e-mail: fusang@iscas.ac.cn).

Daqing Zhang is with the Key Lab of High Confidence Software Technologies (Ministry of Education), School of Computer Science, Peking University, Beijing 100871, China, and also with the Telecom SudParis, Institut Polytechnique de Paris, 91011 Evry Cedex, France (e-mail: dqzhang@sei.pku.edu.cn).

Digital Object Identifier 10.1109/TMC.2024.3450318

diverse diseases [1], [2] and monitoring overall health conditions [3]. For example, according to the latest report from the American Heart Association (AHA), we have seen 928,741 lives lost in the US solely due to cardiovascular disorders in 2020 [4]. We could prevent those tragedies from happening if we could provide robust and accurate continuous heart rate and Heart Rate Variability (HRV) monitoring at home, since rapid or irregular heartbeat is a very critical early symptom of cardiovascular disorders.

Presently, vital sign tracking methods fall into two categories: contact-based and contact-free. Contact-based techniques, including devices like multi-parameter monitors [5], and smart watches [6], necessitate direct bodily contact for proper operation, often leading to user discomfort. Additionally, these devices are ill-suited for long-term patient monitoring due to factors like frequent charging requirements. Among contact-free methods, computer vision based approaches [7] raises severe privacy concerns, notably in bedrooms where privacy is paramount. Radio Frequency (RF) based contact-free vital signs tracking methods have gained increasing attention due to its privacy-preserving nature and sensitivity to subtle movements. These systems utilize wireless signals, such as WiFi [1], UWB [8], and mmWave signal [9], that reflects off the human body to sense minor vibrations induced by breath and the heartbeat within the chest cavity.

In the field of RF-based techniques, human vital sign monitoring systems utilizing mmWave signals have garnered significant interest. This heightened attention can be chiefly attributed to the exceptional sensitivity afforded by mmWave's high frequency and its capacity to offer precise sensing capabilities in terms of both distance and angle dimensions, thanks to its wide GHz-wide bandwidth. Moreover, the well-established commercial viability of mmWave technology plays a pivotal role in this increased focus. Presently, numerous prominent semiconductor manufacturers, such as TI [10], Infineon [11], Calterah [12], and others, have introduced radar chips that are readily available in the commercial market. Consequently, a diverse range of mmWave-based vital sign monitoring systems has showcased remarkable accuracy in controlled laboratory settings using commercial mmWave radar [13].

Despite its success in controlled laboratory environments, the current mmWave-based vital sign monitoring system, especially

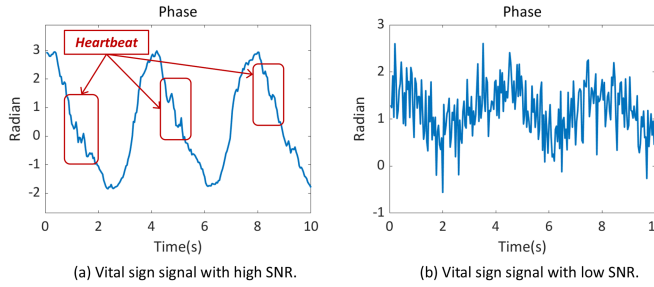


Fig. 1. In low SNR scenarios, noise can obscure the heartbeat signal. Interestingly, these two sets of data are gathered sequentially with a minor body posture adjustment. We term this occurrence the “SNR mutation” phenomenon.

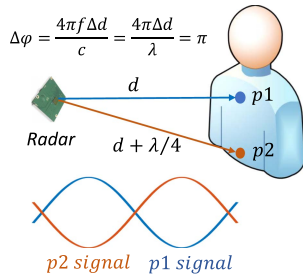


Fig. 2. Intuitive understanding of multi-point reflections. These two signals cancel each other, causing a low SNR.

heartbeat monitoring, encounters a significant challenge when deployed in practical real-world settings: the **SNR mutation**. We refer to the example in Fig. 1 to demonstrate the concept of SNR mutation. In this example, we use mmWave radar to monitor a person’s respiration and heartbeat at two locations separated by just 5 centimeters, and plot the obtained sensing signal in Fig. 1(a) and (b). From Fig. 1(a), we can observe that while the primary variation in the signal is attributed to respiration, the signal fluctuations caused by the heartbeat are still clearly discernible, indicating a high SNR in the sensing signal. Conversely, in Fig. 1(b), noise overwhelms the heartbeat signal, indicating a low SNR in the sensing signal. We refer to this phenomenon, where the SNR of the sensing signal varies significantly with minor motions (e.g. moving 5 centimeters) of the object of interest, as SNR mutation.

SNR mutation arises due to the intricate nature of the human thorax as a signal reflector, reflecting multiple signals rather than the single reflection point assumed in most existing wireless-based human vital sign monitoring systems [1], [13], [14], [15]. The amalgamation of these signal reflections from the human thorax results in intricate signal superimposition. To illustrate this, we can examine the interplay of two signal reflections. As depicted in Fig. 2, a mere quarter-wavelength difference in their travel distances, equivalent to a mere 1.25 mm for the 5 mm wavelength of a 60 GHz mmWave signal, leads to the two signals being out of phase and cancelling each other. Conversely, when two signal reflections travel identical distances before reaching the radar, they reinforce each other upon superposition due to their in-phase nature. This means that even minor body movements can induce significant phase differences between these two reflection point signals, resulting in notable SNR variations in the received sensing signal. Consequently, this dynamic

interplay oscillates between reinforcement and cancellation as body posture changes, giving rise to the phenomenon of SNR mutations. In practical applications, the human thorax involves multiple reflection points, further amplifying the intricacies of this phenomenon.

The phenomenon of SNR mutation poses a significant obstacle to the widespread adoption of mmWave-based heartbeat monitoring systems. In controlled laboratory settings, we can manipulate and maintain the human’s posture to achieve the desired level of accuracy. However, in real-world deployments, the system must exhibit robust performance regardless of the individual’s position and posture. This becomes particularly crucial in scenarios of long-term monitoring of vital signs during human sleep, as people’s sleeping postures unconsciously and continuously change.

In this paper, we propose to leverage frequency diversity to mitigate the impact of SNR mutation. Our fundamental insight lies in the fact that while signal reflections from the human thorax may undergo deconstructive superimposition, leading to cancellation at one frequency, say  $f_1$ , they may concurrently experience constructive superimposition and reinforcement at another frequency, denoted as  $f_2$ . The superimposition of two signals becomes independent from each other only when their frequencies have a large enough gap, denoted as the coherent bandwidth  $f_d = |f_1 - f_2|$ . In this context, we have conducted theoretical derivations to establish  $f_d$  for mmWave-based human vital sign monitoring.

Based on our insights and theoretical results, we have developed a frequency-diversity harnessing algorithm aimed at mitigating SNR mutation. Initially, we introduce a Vital-index metric to evaluate the quality of the received sensing signal at different frequencies, specifically focusing on sensing SNR. Subsequently, we transmit the mmWave signal across multiple frequency bands, each separated by at least the coherent bandwidth  $f_d$ , with the goal of identifying frequencies characterized by constructive signal superimposition and consequently exhibiting higher sensing SNR. Finally, we present a signal combining algorithm designed to optimize sensing SNR by merging signals received from frequencies with robust sensing SNR. Leveraging this improved signal, we can accurately monitor human vital signs, such as respiration and heartbeat, even in the presence of frequent human motions.

In this paper, we design and implement Robust-Vital, a robust long-term vital signs monitoring system using commercial mmWave radars. We recruited 12 volunteers for a comprehensive evaluation of Robust-Vital’s performance in long-term heart rate and heart rate variability tracking. The dataset encompasses over 180 hours of continuous monitoring during the volunteers’ full-night sleep. We used the Interbeat Interval (IBI) as the heart rate variability index. Robust-Vital achieves a median error of 0.36 bpm in heart rate estimation and 5.88ms in IBI estimation, significantly outperforming state-of-the-art method [16] with errors of 2.27 bpm and 33.61 ms, respectively.

The main contributions of our work are summarized as follows.

- For RF-based vital signs tracking, we have, for the first time, developed a multi-point human thorax reflection

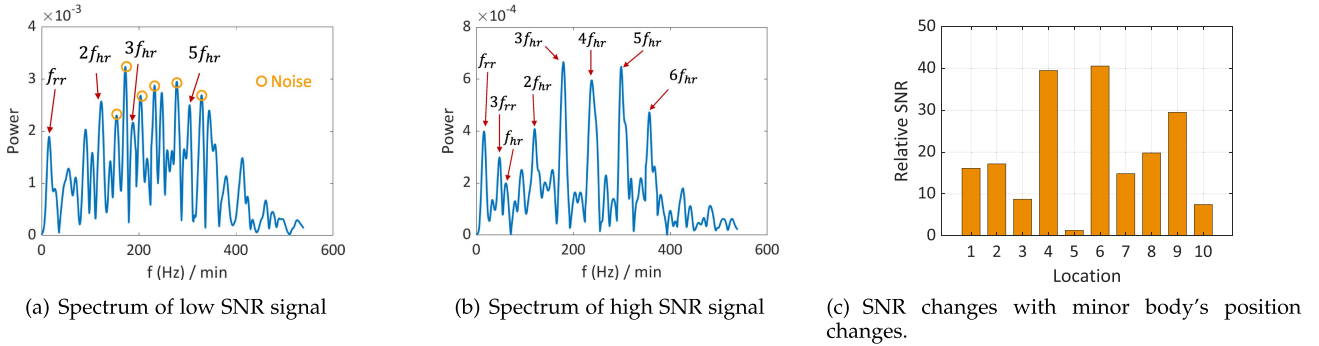


Fig. 3. (a)–(b): Comparison of the spectra of signals with high and low signal-to-noise ratios (SNRs). In the spectrum,  $f_{rr}$  represents respiration rate, and  $f_{hr}$  represents heart rate. (c): In empirical experiments, we observe that small changes in the location of the human body cause large SNR fluctuations.

model to explain factors influencing system robustness and the SNR mutation phenomenon.

- We theoretically derive how minor body posture adjustments and wireless signal carrier frequency changes influence the sensing SNR within the context of the multi-point reflection model.
- We propose a novel signal processing scheme that leverages frequency diversity to improve SNR based on the multi-point reflection model. Our method selects and combines multiple carrier frequencies with superior signal quality, effectively enhancing the robustness of the sensing system.
- We implement Robust-Vital and evaluate its performance through long-term heart rate and HRV tracking. A user study with 12 volunteers demonstrates robust performance over the state-of-the-art solutions.

## II. PRELIMINARIES

In this section, we first introduce the basics of mmWave radar vital sign estimation. Then, we describe the multi-point reflections effect and its impact on the resilience of the sensing system.

### A. Estimating Vital Signs Via Mmwave Radar

The underlying concept for estimating vital signs using wireless technologies is to detect the subtle chest movement induced by respiration and heartbeat. The wireless signal phase associated with the reflection point exhibits a linear change along with the chest displacement in the widely used single-point reflection model:

$$\Delta\varphi = \frac{4\pi f \Delta d}{c} = \frac{4\pi \Delta d}{\lambda} \quad (1)$$

where  $f$  stands for the carrier frequency,  $c$  denotes the speed of light, and  $\lambda$  represents the wavelength. The phase shift  $\Delta\varphi$  is an accurate measure of the change in signal propagation distance,  $\Delta d$  is the displacement of chest movement.

Adults often experience 4 to 12 mm of chest motion from breathing, whereas heartbeat-induced motion is merely around 0.5 mm [17]. Respiration causes significant phase variations that make it easier to be detected using a 60 GHz mmWave radar with

a 5 mm wavelength. Heartbeat, however, causes tiny phase shifts that are sensitive to noise interference, especially in low SNR conditions, as seen in Fig. 1.

Upon acquiring the phase changes, a direct approach for calculating respiratory and heart rates involves filtering signals by certain frequency bands (0.1 to 0.5Hz for breath, 0.8 to 2Hz for heartbeat). Next, strong energy peaks that correlate to respiratory and heart rates are seen within their respective frequency spectra. [14], [18]. To reliably determine the heart rate, however, a number of respiratory harmonics within the heart rate spectrum, such as the third harmonic in Fig. 3(b), provide a considerable challenge. Note that the spectrum in Fig. 3(a) and (b) enhances high-frequency components (associated with heartbeat harmonics) by second-order phase differentiation.

Fortunately, the energy of respiratory harmonics decreases with increasing order, becoming normally less significant after the fourth harmonic. In addition, heartbeat signals contain higher-order harmonics, which are rarely influenced by respiratory harmonics due to their higher frequency, shown in Fig. 3(b). It is straightforward to identify the peaks that correlate to respiration and heartbeat, as well as their harmonics. Fig. 3(a) illustrates how noise could easily submerge heartbeat-related peaks in conditions with lower SNR. As a result, many techniques for calculating heart rate and heart rate variability rely on higher-order heart harmonics [19], [20], [21], [22].

### B. Effect of Multi-Point Reflections on Sensing

Considering the subtle nature of heartbeats, they can be readily obscured by noise in the radar's received signal. SNR thus becomes a critical factor for monitoring heartbeats. SNR in this case refers to the signal-to-noise-ratio (SNR) of the chest-reflected signal received by the radar. SNR is directly proportional to the received signal strength under the assumption that the noise level is constant. If  $R$  denotes the chest-radar distance and  $\lambda$  denotes the wavelength of the transmitted radar signal, under the traditional single-point reflection assumption, the following formula is used to calculate the received signal power [23]:

$$P_r = \frac{P_t G^2 \lambda^2 \sigma}{(4\pi)^2 R^4} \quad (2)$$

where  $P_t$  denotes the transmit power,  $G$  represents the antenna gain, and  $\sigma$  is the radar cross section (RCS).

Note that  $\lambda$ ,  $G$ , and  $P_t$  are typically configured during radar configuration and remain unchanged while the radar is operating. The RCS ( $\sigma$ ) of a target is determined by factors such as the target's material, size, and the angle with the radar. It reflects the radar wave reflection capability of the target. In the single-point reflection assumption, factors such as target size and angle are ignored, keeping the RCS constant for the same target [23]. Thus, under this assumption, the target's SNR is mainly affected by the target-radar distance. When this distance stays constant, the sensing SNR should remain stable.

However, in our empirical studies, we observe that even a slight change in a person's posture can result in a sudden mutation of the SNR. This observation contradicts the conclusions drawn from the single-point reflection assumption. We perform more thorough experiments to examine the underlying reasons. Fig. 15 illustrates the set-up, which comprised a person sleeping on a bed with the radar mounted on the wall above the headboard, about 1.2 meters from the chest. Participants were then instructed to change their position slightly while still remaining supine, and the process was repeated ten times. Notably, these adjustments were considerably minor compared to the radar-chest distance, which remained relatively constant throughout the experiment.

Using our proposed Vital-index metric, which is discussed in Section IV, SNR values at different positions have been obtained. The results of the experiment are shown in Fig. 3(c), which demonstrate large variations in estimated SNR as a function of slight changes in human body position. A major challenge to the robustness of heartbeat detection is posed by the SNR fluctuation because of user's unpredictable and different sleeping positions on the bed. This variation could result in intermittently detectable heartbeats, hindering the realization of long-term robust heartbeat monitoring.

Under the single-point reflection assumption, it is difficult to understand the sudden SNR change. This issue occurs because there are actually multiple reflection points on the target's chest, and the slight movements of the body affect the superposition of these reflection point signals, resulting in significant SNR variations with position changes. In the next section, we will investigate the factors and mechanisms that affect SNR under the multi-point reflection model.

### III. MODELING MULTI-POINT REFLECTIONS ON SENSING TARGET

Recall that our main goal is resolving SNR fluctuation caused by body position adjustments. We have identified the underlying cause of the SNR mutation, which stems from the presence of multiple reflection points on the human chest. The combination manner of signals from these reflection points varies with changes in human body posture, leading to fluctuations in the SNR. Nonetheless, we still lack a quantitative relationship of the variation in human body position required to induce the SNR sudden change.

To tackle SNR fluctuation, we have made an important observation: apart from reflection path lengths, the carrier

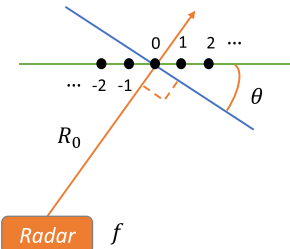


Fig. 4. We represent the reflection of radar waves from the 1D target using a model with  $2M+1$  scatterers and analyze the impact of  $f$  and  $\theta$  changes on SNR.

frequency of wireless signals also affects the phase differences between signals from various reflection points (as per (1)). Signals from multiple reflection points that currently cancel out might potentially be made to strengthen one another by changing the frequency of the transmitted signal. The question of how much frequency change, denoted as coherent frequency ( $f_d$ ), is necessary to do this intuitively follows.

In this section, we investigate the influence of changes in human body position and carrier frequency on SNR within the multi-point reflection model. We begin by quantitatively analyzing these effects for 1D targets. Subsequently, we extend our conclusions to 2D and 3D targets within the context of vital sign monitoring.

#### A. Mechanisms Affecting SNR in Multi-Point Reflection Model

1) *Derivation Methodology:* We first consider the one-dimensional scenario for the target. As illustrated in Fig. 4, we assume that the target consists of point scatterers uniformly spaced at intervals of  $\Delta x$ . We assume a total of  $2M + 1$  scatterers, numbered from  $-M$  to  $M$ , resulting in a total target length of  $L = (2M + 1)\Delta x$ . In the derivation, we employ changes in the angle between the target and the radar line of sight to quantitatively characterize human body displacement, where the angle is represented as  $\theta$ , as shown in Fig. 4.

We expect that the low SNR brought on by human body movement will improve if the carrier frequency is changed. We utilize correlation operations to quantify the extent of signal change. When the carrier frequency changes, if the two signals are highly correlated, they are more similar, and the SNR remains low. In contrast, there is a possibility of changing from a lower SNR to a higher one when the two signals are uncorrelated.

Therefore, our derivation proceeds as follows: Since the received radar signal is the summation of reflections from these scattering points, we calculate the cross-correlation function of the summation signal concerning changes in angle and frequency. This helps us determine the extent of angle or frequency variations required for the summation signal to become decorrelated before and after these changes. In essence, our goal is to find the decorrelation intervals of the summation signal concerning angle and carrier frequency. The decorrelation interval in frequency corresponds to the expected coherent frequency ( $f_d$ ).

2) *Summation of Multi-Point Signal Reflections:* We first derive the signal reflected back from an individual scattering

point in an mmWave radar system and then sum them up to obtain the summation signal.

We assume that the scattering point denoted as “0” in Fig. 4 is located at a distance  $R_0$  from the radar. Then, we can approximate the distance from the radar to the  $n$ -th scattering point as  $R_0 + n\Delta x \sin \theta$ , where  $\Delta x$  is the interval between two adjacent scatterers. This approximation closely resembles the one employed in determining phase differences among diverse antenna paths during angle measurements. Therefore, following the transmission of the radar signal, the delay from the radar to receiving the echo from the  $n$ -th scattering point is  $\tau_n = 2(R_0 + n\Delta x \sin \theta)/c$ .

Assuming the slope of the chirp frequency transmitted by the mmWave radar is represented as  $k$ , the intermediate frequency signal received by the radar from the  $n$ -th scattering point’s reflection is given by [24]:

$$s_n(t) = Ae^{j2\pi(k\tau_n t + f_c \tau_n)} \quad (3)$$

where  $A$  denotes amplitude,  $f_c$  represents the starting frequency, also known as the carrier frequency. Notably,  $s_n(t)$  is the intermediate frequency signal typically utilized for sensing purposes in mmWave radar. Now we sum the signals from the  $2M + 1$  scattering points:

$$\overline{y(t)} = \sum_{n=-M}^M Ae^{j2\pi(k\tau_n t + f_c \tau_n)} \quad (4)$$

$$= \sum_{n=-M}^M Ae^{j2\pi(kt + f_c) \frac{2(R_0 + n\Delta x \sin \theta)}{c}} \quad (5)$$

Moving the terms in the summation that do not depend on ‘ $n$ ’ to the front of the summation:

$$\overline{y(t)} = Ae^{j2\pi(kt + f_c)2R_0/c} \sum_{n=-M}^M e^{j4\pi n \Delta x \sin \theta (f_c + kt)/c} \quad (6)$$

To simplify the notation, define:

$$F = kt + f_c, K_\theta = \frac{2\pi F}{c} \sin \theta = \frac{2\pi}{\lambda} \sin \theta, \alpha = 2\Delta x \quad (7)$$

Here,  $F$  involves frequency-related component, and  $K_\theta$  encompasses both aspect angle ( $\theta$ ) and radar frequency ( $F$ ) that we are interested in. Finally, the summation signal can be simplified as:

$$\overline{y(t; K_\theta)} = Ae^{j2\pi F \frac{2R_0}{c}} \sum_{n=-M}^M e^{j\alpha K_\theta n} \quad (8)$$

**3) Calculating Decorrelation Intervals for Aspect Angle and Radar Frequency:** We note that  $K_\theta$  contains both the aspect angle and radar frequency, and our main focus is the impact on the signal when these two parameters change. Therefore, the problem now shifts to understanding how  $\overline{y(t; K_\theta)}$  is affected by variations in  $K_\theta$ . Hence, we calculate the auto-correlation function of  $K_\theta$  with intervals of  $\Delta K_\theta$ :

$$s_{\bar{y}}(\Delta K_\theta) = \int_{-\pi/\alpha}^{\pi/\alpha} \bar{y}(t; K_\theta) \bar{y}^*(t; K_\theta + \Delta K_\theta) dK_\theta \quad (9)$$

The complex exponential terms outside the summation in (8) can mutually cancel out in (9). Substituting (8) into (9), through

the interchange of integration and summation, and consolidating terms, we derive the:

$$s_{\bar{y}}(\Delta K_\theta) = |A|^2 \sum_{l=-M}^M e^{-j\alpha \Delta K_\theta l} \sum_{n=-M}^M \left[ \int_{-\pi/\alpha}^{\pi/\alpha} e^{-j\alpha(l-n)K_\theta} dK_\theta \right] \quad (10)$$

Introducing a change of variables  $K'_\theta = \alpha K_\theta$  clarifies that the integral resembles the inverse discrete-time Fourier transform of a constant spectrum  $S(K_\theta) = \frac{2\pi}{\alpha}$ . Consequently, the integral simplifies to the discrete impulse function  $\frac{2\theta}{\alpha} \delta[l - n]$ . Leveraging this insight reduces (10) to a single summation over  $l$  that can be computed as follows:

$$s_{\bar{y}}(\Delta K_\theta) = \frac{2\pi |A|^2}{\alpha} \frac{\sin[\alpha(2M+1)\Delta K_\theta/2]}{\sin[\alpha \Delta K_\theta/2]} \\ = \frac{\pi |A|^2}{\Delta x} \frac{\sin[L \cdot \Delta K_\theta]}{\sin[\Delta x \cdot \Delta K_\theta]} \quad (11)$$

The decorrelation interval can now be established by solving (11) to identify the  $\Delta K_\theta$  value that decreases  $s_y$  to a specified level. Subsequently, this  $\Delta K_\theta$  value can be translated into equivalent alterations in frequency or aspect angle. One criterion involves selecting the  $\Delta K_\theta$  value that corresponds to the initial zero of the correlation function, marked by the numerator’s argument reaching  $\pi$  [23]. Utilizing (11) and considering  $L = (2M+1)\Delta x$ , we obtain:

$$\Delta K_\theta = \frac{\pi}{L} \quad (12)$$

Keep in mind that  $K_\theta = (2\pi/c)F \sin \theta$ . The complete differential of  $K_\theta$  is  $dK_\theta = (2\pi/c) \cdot [\sin \theta \cdot dF + F \cos \theta \cdot d\theta]$ . To establish the decorrelation interval in angle for a fixed radar frequency, set  $dF = 0$ , resulting in  $dK_\theta = (2\pi/c) \cdot F \cos \theta \cdot d\theta$ , thus yielding  $dK_\theta = (2\pi/c) \cdot F \cos \theta \cdot \Delta\theta$ . Likewise, to achieve signal decorrelation, we determine the necessary frequency step by maintaining a constant aspect angle  $\theta$ , resulting in  $dK_\theta = (2\pi/c) \cdot \sin \theta \cdot \Delta F$ . When combining these relations with (12), we derive the necessary changes in aspect angle and frequency to achieve decorrelation of the radar signal amplitude.

$$\Delta\theta = \frac{c}{2F \cdot L \cos \theta}, \quad f_d = \Delta F = \frac{c}{2L \sin \theta} \quad (13)$$

It’s worth noting that  $L \cos \theta$  represents the target’s extent projected perpendicular to the radar boresight, whereas  $L \sin \theta$  represents the projection along the radar’s boresight. As a result, the decorrelation interval in aspect angle is determined by the target’s width as viewed from the radar, while the interval in frequency is driven by the depth.

**4) Decorrelation Intervals in Vital Sign Monitoring Scenarios:** In the context of vital sign monitoring, as illustrated in Fig. 5, a person lies in bed with a 60 GHz mmWave radar mounted on the wall above the headboard. The radar observes the person’s chest at a 45-degree angle, with the chest size approximately measuring 0.5 meters. Using (13), we can compute a decorrelation interval of 0.4 degrees and a decorrelation frequency of 0.42 GHz.

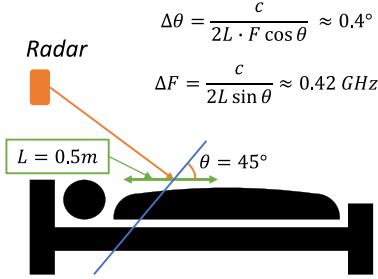


Fig. 5. A slight  $0.4^\circ$  change in  $\theta$  could switch SNR between good and poor. A 0.42 GHz frequency change might also toggle SNR between good and poor.

A 0.4-degree angle decorrelation interval implies that a mere 0.4-degree shift in the radar's viewing angle, caused by human motion, disrupts the correlation between signal amplitudes before and after this shift. Notably, this 0.4-degree change is exceptionally sensitive, as even minor body movements can achieve such an alteration. In essence, the SNR is initially high when there's no bodily motion, but even a slight movement can significantly reduce the SNR. This provides a theoretical explanation for the SNR mutation phenomenon.

A 0.42 GHz frequency decorrelation interval means that, even when the human body is stationary, shifts in the radar signal's carrier frequency greater than 0.42 GHz can significantly impact the signal's SNR. Our mmWave radar, with a bandwidth of up to 4 GHz, easily accommodates a 0.42 GHz frequency shift. This forms the basis of our strategy to mitigate the SNR fluctuations caused by human motion and enhance the robustness of heartbeat monitoring.

### B. Simulation Validation for Vital Sign Monitoring Scenarios

The preceding section's derivation established a solid theoretical basis for comprehending the factors influencing SNR arising from variations in both human body position and radar carrier frequency. This theoretical framework provides essential guidance for our experimental work. However, the previous derivation was grounded in ideal one-dimensional target scenarios, whereas practical situations involve two or three-dimensional targets. In this section, we will demonstrate simulation outcomes for 2D and 3D scenarios, employing vital sign monitoring as an example.

We begin with simulations in a two-dimensional scenario. The simulation setup is similar to Fig. 5, where we assume the human chest is a  $30\text{ cm} \times 50\text{ cm}$  plane. Next, we hypothesize the presence of 15 scattering points uniformly distributed across this plane. Subsequently, we compute the sum of signals received by the radar from these scattering points. Assuming a constant noise level, the SNR is proportional to the power of the received signal. We systematically vary the radar's carrier frequency and human body position to observe how the relative SNR changes. It's worth noting that the magnitude of simulated human body position variations is on the order of a few centimeters.

The results are shown in Figs. 6 and 7. We observe that even slight movements of the human body can cause substantial changes in SNR, in line with our theoretical predictions.

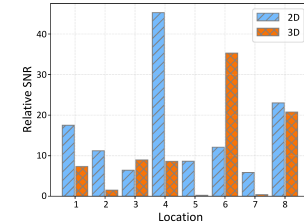


Fig. 6. Simulation results for SNR fluctuations with minor changes in human body position.

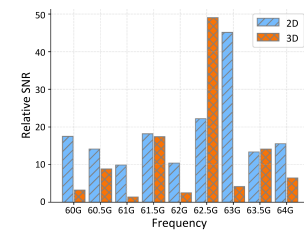


Fig. 7. Simulation results for SNR fluctuations with changing carrier frequency.

Furthermore, when the carrier frequency exceeds the theoretically calculated 0.42 GHz, the SNR shows significant fluctuations, consistent with our theoretical expectations.

To approach a more realistic scenario, we also conducted simulations in a three-dimensional context. We modeled the human chest as a semi-cylinder with a diameter of 15cm and a height of 50 cm. Then, we evenly distributed 15 scattering points on the surface of this semi-cylinder. The remaining settings were similar to the 2D simulations. The simulation results are presented in Figs. 6 and 7, and the conclusions are consistent with those of the 2D scenario.

The simulation results in both 2D and 3D scenarios validate the applicability of our theoretical derivations. They also confirm the potential to enhance the robustness of heartbeat monitoring by varying the carrier frequency in response to the low SNR caused by human body movement. In the next section, we will propose specific methods based on the conclusions drawn in this section.

## IV. ROBUST-VITAL DESIGN: LEVERAGING FREQUENCY DIVERSITY

This section introduces the design of Robust-Vital. Robust-Vital achieves long-term robust tracking of vital signs by leveraging the frequency diversity of the mmWave radar. Fig. 8 shows the system overview of Robust-Vital, which involves three main modules:

- *Data Collection:* In this module, we utilize mmWave radar for capturing signals associated with human vital signs. These signals are then forwarded to the high SNR generation module in the form of Intermediate Frequency (IF) signals.
- *High SNR Signal Generation:* This module takes IF signals as input and outputs a composite signal of vital signs with a

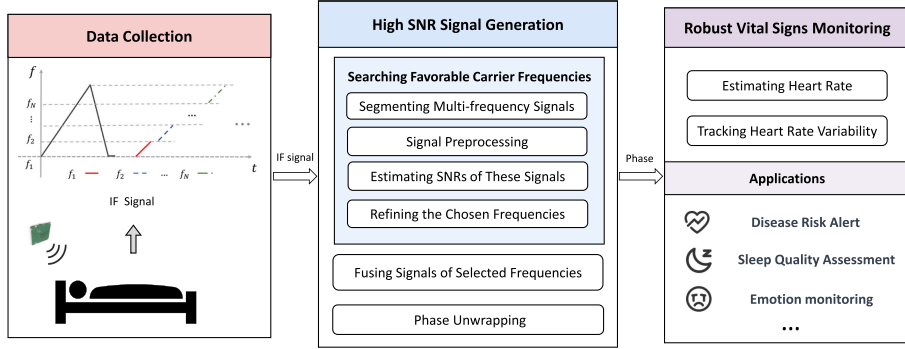


Fig. 8. System overview of Robust-Vital.

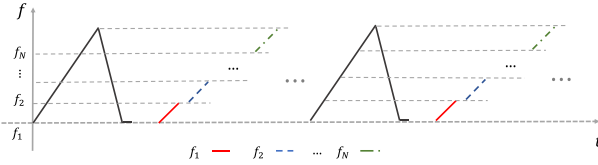


Fig. 9. The implementation of frequency diversity based on time-division multiplexing by segmenting chirp signals.

high SNR. This process involves initially acquiring multi-frequency signals, followed by using our proposed Vital-index metric to identify several carrier frequencies with favorable SNRs. These selected signals are then combined to obtain a high SNR signal, preparing it for vital sign extraction.

- *Robust Vital Signs Estimation:* This module estimates vital signs of the human body based on the high SNR signal. The vital signs encompass respiration rate, heart rate, and heart rate variability.

#### A. High SNR Signal Generation

This module involves first acquiring signals at multiple frequencies. We then utilize our proposed Vital-index metric to identify and retain carrier frequencies with higher SNRs, discarding those with poorer SNRs. Subsequently, these selected signals are combined to obtain a more higher SNR signal, preparing it for vital sign estimation.

1) *Segmenting Favorable Carrier Frequencies:* To search for carrier frequencies with favorable SNRs, we first need signals at multiple frequencies. However, the modulation scheme of mmWave radar currently cannot simultaneously transmit signals at different frequencies. Therefore, our key insight behind obtaining multi-carrier frequency signals is to use time-division multiplexing by segmenting chirp signals.

As depicted in Fig. 9, we segment a sampled chirp signal based on our specified starting frequency and bandwidth. Since the time intervals between the resulting N sub-chirps are extremely short, they can be treated as simultaneously transmitted. Applying this method to each chirp enables us to acquire sampled vital sign signals at N carrier frequencies.

In practice, we utilized the Calterah radar CAL60S244 [12], operating in the frequency range of 60 to 64 GHz. To identify high SNR carrier frequencies within its operational bandwidth, we employed two different bandwidth settings: 0.5 GHz and 0.8 GHz. For the 0.5 GHz bandwidth, we selected starting frequencies ranging from 60 GHz to 63.5 GHz, with increments of 0.5 GHz. Consequently, we obtained a total of 8 signals with different frequencies. For the 0.8 GHz bandwidth, we selected starting frequencies ranging from 60 GHz to 63.2 GHz, with increments of 0.8 GHz. This yielded a total of 5 signals. In total, we acquired 13 signals with different frequencies and bandwidths. We opted for narrower bandwidths because larger bandwidths increase the likelihood of including carrier frequencies with lower SNRs.

We acknowledge that the method of segmenting the IF signals reduces effective bandwidth, thereby affecting range resolution. However, in vital signs monitoring, bandwidth is not a critical metric, as its size does not impact the radar's ability to capture subtle chest movements.

2) *Signal Preprocessing:* Signal preprocessing involves utilizing 1D FFT to process the IF signal into individual range bins. Subsequently, beamforming is performed using a 4-transmit, 4-receive antennas in the Calterah radar to enhance the SNR.

For each frequency, we obtain complex signal variations over time that are associated with vital signs. This is achieved by performing a 1D Fast Fourier Transform (FFT) on each chirp and then extracting the signal from the target range bin, as detailed in [25]. The projection of the complex signal along the time dimension on the IQ complex plane is illustrated in Fig. 10(a). The complex signals displayed in the Fig. 10(a) represent dynamic signals after static removal using circular fitting [25]. We can observe that the complex vector undergoes rotation in response to chest vibrations. The phase changes over time of the complex vector are shown in Fig. 10(b). We also employed the common multi-antenna-based beamforming technique to enhance the SNR for each carrier frequency [9].

3) *Evaluating SNRs of the Multi-Frequency Signals:* Among all carrier frequencies, some exhibit high SNR, while others have low SNR. Our objective is to retain the good ones and discard the poor ones. Consequently, SNR calculations are necessary for each carrier frequency. However, due to the mixture of noise and signal, accurately segregating their energies is challenging,

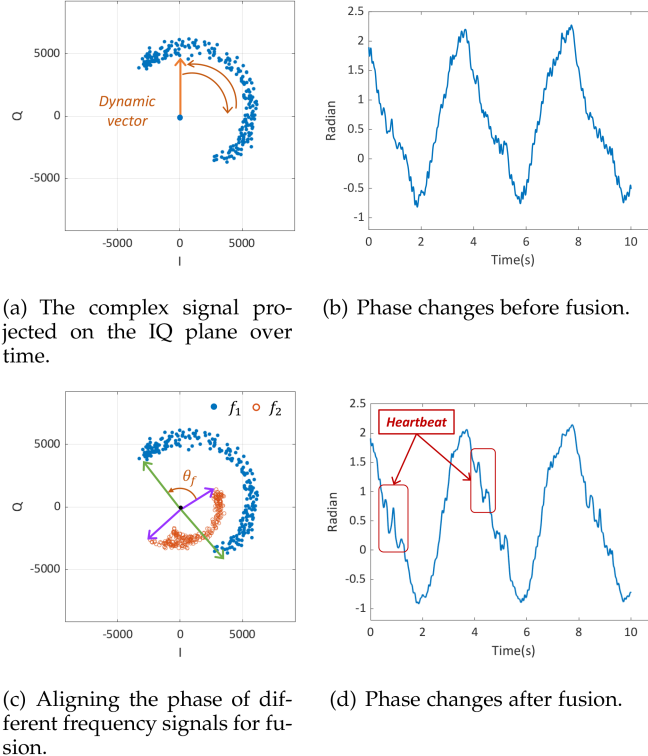


Fig. 10. High SNR signal generation. (c) Shows two signals at different frequencies, selected using our Vital-index for their high SNR. To fuse them, we align the phases of these signals. (d) Demonstrates that after fusion, the phase quality is notably improved compared to before fusion (b), resulting in a clearer representation of the heartbeat signal.

making direct SNR computation difficult. Therefore, we propose the Vital-index (VI) as an approximation for SNR in vital sign monitoring scenarios.

During vital sign monitoring, dynamic signals primarily result from respiration, leading dynamic vectors to oscillate within the complex plane. At this stage, the endpoint of the dynamic vector forms an arc, as depicted in Fig. 10(a), where the signal's magnitude corresponds to the arc's radius. Due to the presence of noise, the distances of sampled points from the arc's center don't precisely match the radius. When all the points' distances to the center are closer to the radius, it indicates that these points are tightly distributed around the arc, implying lower noise. Conversely, in the presence of higher noise, the discrepancies between these distances and the radius increase. Hence, we opt to quantify noise energy using the variance of these distances from the radius. The larger the noise, the greater the variance.

Assuming there are  $K$  complex samples within a time window, Vital-index (VI) can be computed as follows:

$$VI = \frac{(\frac{1}{K} \sum_{i=1}^K |CS(i)|)^2}{var(|CS|)} \quad (14)$$

where  $CS$  denotes the complex signal in the time window. Since  $CS$  is the complex signal after static clutter removal, the center of the arc corresponds to the origin of the coordinate axis. Therefore, we estimate the signal's magnitude by using the average distance of these sampled points to the origin.

The Vital-index we propose is only an approximation of the SNR. This is because the variance of the absolute values of  $CS$  does not represent the energy of complex signal noise but rather the energy of this noise in the one-dimensional projection along the radial direction, providing an approximate value. The noise energy of the complex signal cannot be accurately calculated, because it is impossible to determine the precise position of the dynamic vector at each moment. We will demonstrate the effectiveness of this metric in the evaluation section.

**4) Refining the Chosen Frequencies:** Using the Vital-index, we can evaluate the SNR of the 13 different carrier frequency signals generated in Section IV-A1. In our dataset, we have observed that signal quality is good when the Vital-index exceeds 50, and moderate when it surpasses 25. However, when this index drops below 25, signal quality significantly deteriorates, posing challenges for robust heart rate monitoring. Our strategy for retaining signals with good SNRs is to keep all carrier frequencies with a Vital-index exceeding 50. If the number of carrier frequencies exceeding 50 does not exceed four, we supplement them with frequencies with Vital-index values greater than 25, in descending order, until we reach four frequencies. If we still don't have four carrier frequencies after supplementation, we do not continue to supplement further; we retain the number we have.

Because the starting frequencies of the thirteen carrier frequency signals generated in Section IV-A1 are fixed and have certain intervals, the selected carrier frequencies around them may not necessarily be optimal. Slight adjustments to their starting frequencies could potentially yield signals with better signal-to-noise ratios. Therefore, in this subsection, we make refinements to the selected carrier frequencies.

For each selected carrier frequency, we maintain its bandwidth while varying its starting frequency within  $\pm 0.2$  GHz of its original frequency in 0.1 GHz steps. For example, for a signal with a starting frequency of 61 GHz, we can obtain an additional four frequencies: 60.8 GHz, 60.9 GHz, 61.1 GHz, and 61.2 GHz. We then use the Vital-index to select the carrier frequency with the best SNR as the refined carrier frequency.

**5) Fusing Signals of Selected Frequencies:** The key to merging multiple signals lies in aligning the phases of these signals [23], [26], ensuring that they are in phase with each other to enhance mutual reinforcement during superposition. Using the two signals illustrated in Fig. 10(c) as an example, the fusion process hinges on determining an angle, denoted as  $\theta$ , such that rotating the orange signal at carrier frequency  $f_1$  by this angle aligns it in phase with the blue signal at carrier frequency  $f_2$ . Once phase alignment is achieved, the signals can be added together to enhance the SNR.

Mathematically, this rotation is achieved by multiplying the signal  $CS_2$  by  $e^{j\theta_f}$ , where  $CS_{f_2}$  denotes the signal at carrier frequency  $f_2$ . Therefore, the summation signal can be expressed as:

$$SC(i) = CS_{f_1}(i) + CS_{f_2}(i) \cdot e^{j\theta_f}, i = 1 \dots K \quad (15)$$

where  $SC$  denotes the summation complex signal. So, the remaining question becomes how to determine  $\theta_f$ .

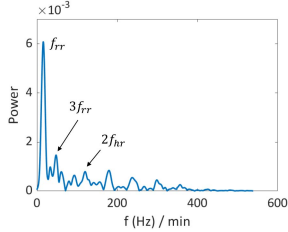


Fig. 11. Spectrum of the phase. Respiration rate (rr) can be easily solved.

We treat the problem as an optimization task by searching for the angle  $\theta_f$  that maximizes the dynamic energy of  $SC$ . The definition of dynamic energy here is the summation of the amplitudes of all sampled points after static removal, that is, the amplitude of dynamic vector [9]. The dynamic energy after signal addition is maximized only when the two signals are completely in phase with each other. Therefore, the optimization function is formulated as follows:

$$\max_{\theta_f} Dyn(SC) = \sum_{i=1}^K |CS_{f_1}(i) + CS_{f_2}(i) \cdot e^{j\theta_f}| \quad (16)$$

We performed a search with a step size of  $1^\circ$ , iterating from  $0^\circ$  to  $360^\circ$ . We also explored other optimization objectives, such as maximizing the energy in the frequency band corresponding to the heartbeat, and found that the results were similar to maximizing dynamic energy.

The technique for combining signals from two carrier frequencies has been outlined earlier. Extending this approach to fuse multiple signals proceeds similarly. We designate one carrier frequency as the reference signal and align the phases of the other carrier frequencies' signals with the reference signal by employing the previously discussed rotation angle determination method. Ultimately, these phase-aligned signals are straightforwardly summed to produce the ultimate high SNR signal. Fig. 10(d) displays the phase extracted from the superimposed signal fused from signals of five carrier frequencies. As compared to Fig. 10(b), it's evident that noise in the signal has significantly attenuated, and the signal related to the heartbeat is more clearly manifested.

### B. Robust Vital Signs Estimation

Our target vital signs encompass three aspects: respiratory rate, heart rate, and heart rate variability (HRV). HRV extraction is motivated by the fact that a healthy heart does not beat at regular intervals [27]. In essence, the patterns of a healthy heart are nonlinear and provide higher-dimensional information compared to heart rate, which is more stable. We employ the Interbeat Interval (IBI) as the HRV index.

1) *Heart Rate and Respiration Rate Estimation:* Calculating the respiratory rate is straightforward. We begin by performing an FFT on the phase of the fusion signal, resulting in the spectrum shown in Fig. 11. By seeking peaks within the frequency range associated with respiratory rate, the highest peak is pinpointed, representing the respiratory rate. Our selected

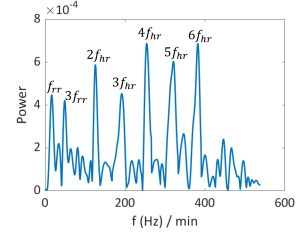


Fig. 12. Spectrum of the second-order phase difference.  $f_{hr}$  denotes heart rate.

frequency range for respiratory rate is 8 to 35 breaths per minute (bpm).

Given the vulnerability of the fundamental heart rate frequency to respiratory harmonics interference [19], [28], [29], we opt to compute the heart rate using its harmonics, which exhibit higher frequencies. To achieve this, we apply a second-order difference to the phase signal before its transformation into the frequency domain. This second-order difference essentially serves as a high-pass filter [30]. The resultant phase spectrum after this difference is illustrated in Fig. 12, allowing for the clear identification of peaks associated with different heart rate harmonics.

Our heart rate calculation process comprises two steps. First, we identify the strongest harmonic of the heartbeat. Second, we determine the heart rate by associating it with the corresponding harmonic of the heartbeat. Our heart rate measurement range is from 50 to 120 beats per minute (bpm). In the first step, we search for the strongest peak within the range of 100 to 245 bpm. This peak's frequency may correspond to the 2nd, 3rd, or 4th harmonic of the heartbeat, denoted as  $f_{har}$ .

Next, we will utilize the peaks of the remaining heart rate harmonics to assist us in determining which harmonic of the heartbeat corresponds to  $f_{har}$ . Specifically, we search for the three strongest peaks, excluding  $f_{har}$ , within the range of 100 bpm to 480 bpm, as these peaks are likely to be harmonics of the heartbeat. These peaks correspond to frequencies denoted as set:

$$F = \{f_{hi} | i = 1, 2, 3\} \quad (17)$$

Then, we sequentially assume  $f_{har}$  to be the second, third, and fourth harmonic of the heartbeat and calculate the heart rate for each assumption:

$$f_k = f_{har}/k, \quad k = 2, 3, 4 \quad (18)$$

We identify all harmonics of  $f_k$  between 100 bpm and 480 bpm, denoted as set  $H_k$ . Then, we calculate the error between  $H_k$  and  $F$ , with the aim of minimizing this error to determine the harmonic frequency of  $f_{har}$ . Our method for calculating the error between  $H_k$  and  $F$  is as follows: for each element in  $F$ , we find the closest value in  $H_k$ , and the difference between these values is considered the error. By iterating through each element of  $F$  and summing the errors, we obtain the total error between  $H_k$  and  $F$ , denoted as  $e_k$ .

$$k^* = \arg \min_k e_k \quad (19)$$

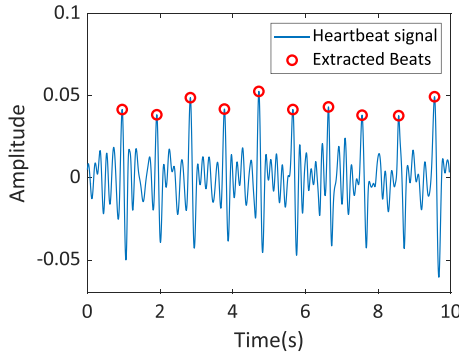


Fig. 13. Recovered heartbeat signal and extracted timings of each beat.

where  $k^*$  represents the most probable number of heartbeat harmonics for  $f_{har}$ . Therefore, the heart rate can be calculated as:

$$f_h = f_{har}/k^* \quad (20)$$

*2) Interbeat Interval Segmentation:* To extract the interbeat interval, we employ the VMD algorithm, which decomposes the phase signal into distinct modes known as Intrinsic Mode Functions (IMFs) through variational calculus [15], [31]. Each IMF is centered around a specific frequency with a narrow bandwidth. These separated IMFs correspond to the fundamental components of respiration and heartbeat, as well as their respective harmonics [15], [32].

Since we already know the heartbeat's frequency, we can identify the IMFs corresponding to each harmonic of the heartbeat and sum them to obtain the heartbeat's time-domain waveform, as depicted in Fig. 13. IBIs depend on the timing of each heartbeat, which we determine by detecting peaks in the heartbeat signal. Because within a heartbeat signal, apart from the strongest peak, numerous smaller peaks should not be detected. We establish a minimum time gap between the two peaks based on the heart rate. The minimum interval is set to 70% of the average time between heartbeats using the heart rate. The output of our peak detection algorithm is displayed in Fig. 13, demonstrating precise recovery of beat timings.

## V. EVALUATION

In this section, we evaluate Robust-Vital's performance by conducting long-term experiments in real-world home environments. We evaluate Robust-Vital on different environments, participants, and radars. Over 180 hours of data substantiate the robustness of Robust-Vital in monitoring heart rate and heart rate variability.

### A. Experiment Setup

*1) Implementations:* Our system utilizes Calterah's CAL60S244-IB radar sensor chip, which features a 4 TX and 4 RX antenna array [12]. This chip integrates a single-chip FMCW radar sensor designed for operation in the 60 to 64 GHz band. Fig. 14 provides a visual representation of the physical appearance of the CAL60S244-IB radar device and

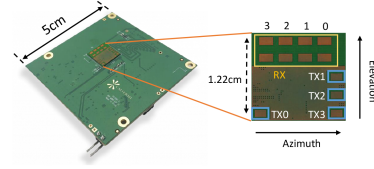


Fig. 14. The mmWave radar. [12].



Fig. 15. Monitoring scenario.

the arrangement of its antenna array. The radar sends 1000 chirps per second, with each chirp having a duration of 60  $\mu s$ . The data processing occurs on a ThinkPad laptop equipped with an Intel i7-8750H processor and 16 GB of memory. The window we set for computing vital signs is 10 seconds. Signal processing is implemented using Matlab. The radar's sampled data is transmitted to the laptop via a TCP connection upon capturing reflection signals.

*2) Data Collection:* The data collection setup is shown in Fig. 15, with the radar mounted on the wall beside the bed to monitor sleeping individuals' vital signs. Ground truth data was recorded using the Heal Force PC-3000 multi-parameter monitor, capable of tracking vital signs like respiration rate and ECG data. The ECG data is subsequently processed to extract heart rate and heart rate variability. We recruited a total of 12 volunteers, including 4 females, to collect data in four different rooms. All volunteers are fully informed about the experimental content and participate voluntarily. Robust-Vital operated during the volunteers' overnight sleep, yielding 27 nights of data and over 180 hours of experimentation.

### B. Overall Performance

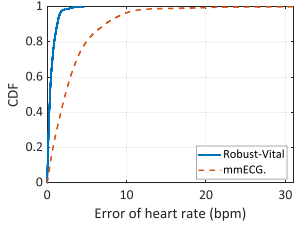
*1) Evaluation of Heart Rate and Respiration Rate Monitoring:* The heart rate estimation error is defined as the absolute difference between the estimated heart rate ( $H_E$ ) and the actual heart rate ( $H_A$ ), that is,  $|H_E - H_A|$ . We evaluate the heart rate estimation performance of Robust-Vital in comparison to mmECG. [16]. mmECG is one of the state-of-the-art research proposals that utilize mmWave radar for heart rate estimation in low SNR conditions. Fig. 16(a) shows the Cumulative Distribution Function (CDF) of heart rate estimation errors across all experiments. Robust-Vital achieves a median error of 0.36 bpm. In comparison, mmECG's [16] median error in heart rate is 2.27 bpm, with a relatively long tail, indicating vulnerability to SNR fluctuations.

The respiration rate estimation error is defined as the absolute difference between the estimated respiration rate ( $R_E$ ) and the actual respiration rate ( $R_A$ ), that is,  $|R_E - R_A|$ . We evaluate

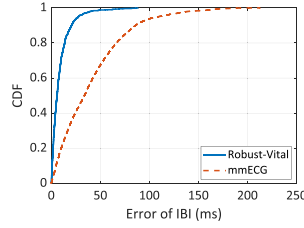
TABLE I  
COMPARISON OF ROBUST-VITAL PERFORMANCE ACROSS VARIOUS USERS

User	Age	Gender	Weight (kg)	Height (cm)	Heart rate MAE (bpm)	IBI MAE (ms)
1	24	M	56	178	0.37	5.96
2	24	M	65	173	0.35	5.83
3	25	M	71	174	0.35	5.81
4	23	F	51	164	0.37	6.03
5	29	M	82	182	0.36	5.85
6	25	F	50	162	0.37	6.39
7	39	M	58	177	0.35	5.85
8	48	F	64	169	0.34	5.51
9	47	F	66	165	0.36	5.80
10	27	M	87	186	0.32	5.44
11	56	M	60	167	0.35	5.71
12	26	M	73	173	0.37	6.17

MAE is an abbreviation for median absolute error.



(a) CDF of heart rate estimation error.



(b) CDF of the IBI estimation error.

Fig. 16. Overall performance of Robust-Vital.

the respiration rate estimation performance of Robust-Vital in comparison to Ahmad et al. [18]. Because of the substantial amplitude of respiratory movement, it is minimally impacted by SNR fluctuations. Hence, traditional mmWave radar methods can proficiently determine the user’s respiration rate. Ahmad et al. [18] is considered a classic and state-of-the-art approach in wireless signal based respiration rate monitoring. Robust-Vital achieves a median error of 0.18 bpm. As a comparison, the median error of respiration rate of Ahmad et al. is 0.23 bpm. As our primary focus is on the robustness of heartbeat monitoring, we will no longer report the evaluation of respiration in the upcoming sections.

2) *Evaluation of Heart Rate Variability Tracking*: Next, we evaluate Robust-Vital’s heart rate estimation performance in comparison to mmECG [16]. mmECG is a state-of-the-art work that utilizes the VMD algorithm to recover the time-domain waveform of the heartbeat and then estimate heart rate variability. We employ the Interbeat Interval (IBI) to evaluate Robust-Vital’s heart rate estimation performance. Fig. 16(b) demonstrates the CDF of IBI measurement errors across all experiments. We can see that Robust-Vital achieves a median error of 5.88 ms for the IBI of the users. In contrast, mmECG exhibits a significantly higher median error of 33.61 ms, indicating inferior performance compared to our system. This outcome underscores Robust-Vital’s ability to robustly adapt to various scenarios during actual user sleep when estimating heart rate variability.



Fig. 17. Pictures of four different bedrooms.

### C. User and Environment Factors Study

We evaluate several practical factors that may influence the applicability of Robust-Vital in real-world scenarios.

1) *Impact of Different Users*: To evaluate the performance of Robust-Vital across various users, we recruited 12 participants (including 4 females). The participants’ ages ranged from 20 and 56 years ( $\mu = 32.75$ ), with weights between 50 and 87 kg ( $\mu = 65.25$ ), and heights ranging from 162 and 186 cm ( $\mu = 172.5$ ). During the experiments, these participants wore their regular sleepwear and slept normally without any additional requirements. They were free to sleep in their preferred positions and follow their usual sleep habits.

The experimental results involving different users and Robust-Vital are summarized in Table I. We provide information on the physical characteristics of each individual, along with the median error in heart rate and IBI estimation for each participant. These results demonstrate that Robust-Vital consistently performs well across diverse individuals, regardless of factors like height, weight, gender, and more.

2) *Impact of Different Rooms*: To get the best performance of Robust-Vital, we study the impact of different rooms by deploying Robust-Vital in four different bedrooms, as shown in Fig. 17. In all four environments, this is common furniture, such as beds, desks, chairs, and wardrobes. These four different bedrooms vary in terms of their size, layout, as well as the size and placement of the beds. Consequently, this results in varying distances between the radar and the individuals lying on the bed, ranging from 0.8 meters to 1.5 meters.

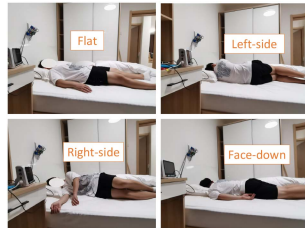
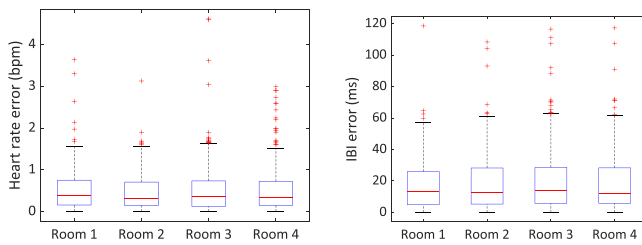
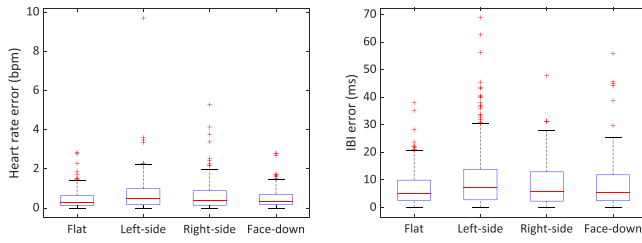


Fig. 18. Pictures of four different sleeping postures.



(a) Box plot of heart rate estimation error. (b) Box plot of IBI estimation error.

Fig. 19. Robust-Vital performance across different rooms.



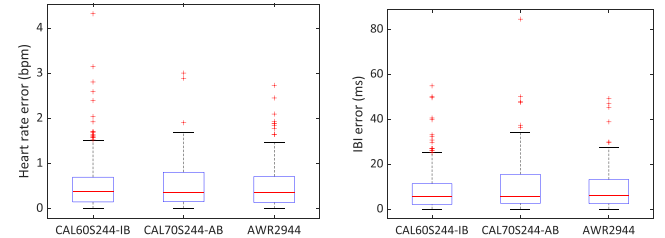
(a) Box plot of heart rate estimation error. (b) Box plot of IBI estimation error.

Fig. 20. Robust-Vital performance across sleeping postures.

Fig. 19(a) and (b) show the errors in heart rate estimation and IBI estimation, respectively. In detail, the median heart rate estimation errors for the four rooms are 0.38, 0.32, 0.37, and 0.33 bpm, respectively. The IBI estimation errors for these rooms are 5.95, 5.82, 6.32, and 5.48 ms, respectively. This demonstrates that Robust-Vital's performance generalizes well across different rooms.

**3) Impact of Different Sleeping Postures:** Since individuals' sleeping positions are uncontrolled and variable, they may sleep in a flat, side, or even face-down position. These variations result in differences in the chest area exposed to radar waves, with larger areas when lying flat or face down. Furthermore, different parts of the chest cavity experience varying degrees of movement due to vital signs, leading to variations in signal fluctuations. Therefore, we evaluate Robust-Vital's performance under different sleeping postures by categorizing them into four types: flat, left-side, right-side, and face-down posture, as shown in Fig. 18.

Fig. 20(a) and (b) illustrate errors in heart rate and IBI estimation for four different sleeping postures. We observe



(a) Box plot of heart rate estimation error. (b) Box plot of IBI estimation error.

Fig. 21. Robust-Vital performance across different radar devices.

minor error variations among these postures. Flat and face-down sleeping show lower errors, followed by right-side sleeping, while left-side sleeping displays the largest error. Specifically, median heart rate estimation errors for flat, left-side, right-side, and face-down sleeping are 0.31, 0.48, 0.37, and 0.33 bpm, respectively. The corresponding IBI estimation errors are 5.23, 7.17, 5.90, and 5.53 ms.

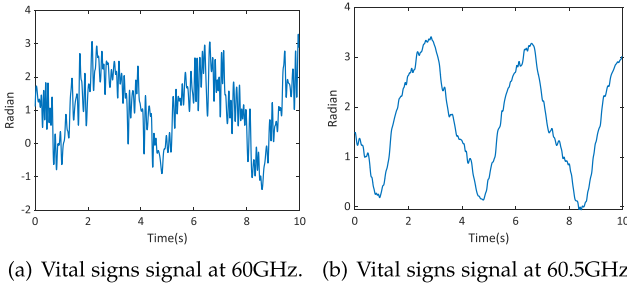
Flat and face-down positions offer larger reflective areas, resulting in better SNRs and improved performance. Conversely, left-side sleeping, with the heart positioned on the left side, leads to smaller vibrations sensed by the radar on the right side of the chest cavity, resulting in lower SNRs and increased susceptibility to noise interference. Despite the larger errors during left-side sleeping, the heart rate error of 0.48 bpm and IBI estimation error of 7.17 ms remain within an acceptable range, significantly surpassing current state-of-the-art methods. Therefore, these experimental findings affirm the effective performance of Robust-Vital across diverse sleeping postures.

**4) Impact of Different Radar Devices:** Radar models of different types may exhibit variations in performance due to differences in carrier frequencies and manufacturers. To assess the system's adaptability to different devices, we conducted evaluations with two additional radar models, CAL70S244-AB (manufactured by Calterah) [12] and AWR2944 (from Texas Instruments) [10]. The CAL70S244-AB radar operates within the 76 GHz to 81 GHz frequency range, while the AWR2944 is a Texas Instruments mmWave radar with the same frequency range.

Fig. 21(a) and (b) present the heart rate and IBI estimation errors for these three radar products. Specifically, for the CAL60S244-IB, CAL70S244-AB, and AWR2944 radar models, the median errors in heart rate estimation are 0.37, 0.35, and 0.36 bpm, respectively, and the errors in IBI estimation are 5.79, 5.48, and 6.07 ms, respectively. Our findings reveal that LoCal consistently performs well across all three radar models, demonstrating the system's ability to generalize effectively to various radar devices.

#### D. Multi-Point Reflection Model Study

The essence of Robust-Vital is to enhance the robustness of the sensing system by leveraging the varying SNR at different carrier frequencies within a multi-point reflection model. Thus,



(a) Vital signs signal at 60GHz. (b) Vital signs signal at 60.5GHz.

Fig. 22. The vital signs signal at different frequencies.

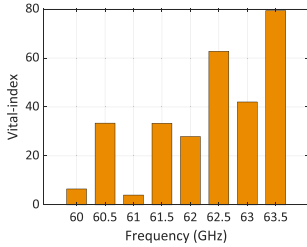


Fig. 23. Results of Vital-index changes with frequency.

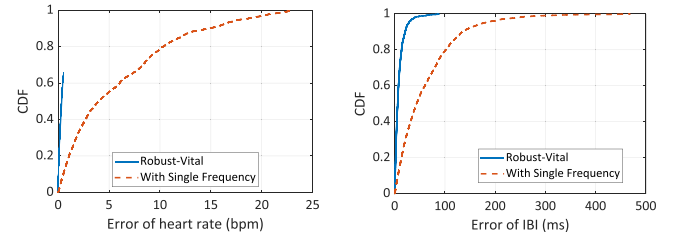
in this subsection, we verify the correctness of the multi-point reflection model.

As introduced in Section III, under the multi-point reflection model, we established the conclusion that variations in both human body position and signal carrier frequency can induce changes in the SNR. Therefore, we validate the correctness of the multi-point reflection model and its conclusions by observing whether the SNR exhibits significant changes as expected when human body position or signal carrier frequency is altered.

We have empirically validated the impact of slight variations in human body position on the SNR in Section II-B. Now, we investigate the influence of changing the signal carrier frequency while keeping the human body position stationary. The experimental setup remains consistent, with a subject lying motionless on a bed. The experimental results are presented in Fig. 22. Fig. 22(a) and (b) display radar signals at 60 GHz and 60.5 GHz, revealing noticeable differences in their SNRs. This observation is in line with our theoretical derivation of a decorrelation interval of 0.42 GHz. Additional frequency data is shown in Fig. 23. We can observe that the SNR undergoes random fluctuations as the frequency changes. Combining the results from Section II-B, we can conclude that the experimental observations align with the theoretical predictions, thus confirming the correctness of the multi-point reflection model.

#### E. Ablation Study

Since the core module of Robust-Vital crucial for enhancing robustness relies on multi-frequency signal processing, we illustrate its significance in the system by conducting ablation experiments and comparing it with experiments using only single-frequency signals.



(a) CDF of heart rate estimation error. (b) CDF of IBI estimation error.

Fig. 24. Ablation study of Robust-Vital.

We used a single-frequency signal at 60 GHz. Fig. 24(a) illustrates the comparison of heart rate estimations. It's clear that using only a single-frequency signal results in a consistent decline in heart rate estimation quality. More precisely, the median error in heart rate estimation with a single-frequency signal is 3.06 bpm, which is considerably worse than Robust-Vital's 0.36 bpm. These findings highlight the substantial improvement in robustness for heart rate estimation brought about by our multi-frequency signal based SNR enhancement module.

Fig. 24(b) illustrates a comparison between IBI estimation using a single-frequency signal and Robust-Vital. The superiority of Robust-Vital, which utilizes multi-frequency signals, is evident, as it substantially reduces errors compared to single-frequency signal usage. Specifically, the median error in IBI estimation using a single-frequency signal is 44.05 ms, significantly higher than Robust-Vital's 5.88 ms. These results, combined with the heart rate estimation comparison, confirm that the multi-frequency signal based SNR enhancement technique significantly improves the robustness of the Robust-Vital, as demonstrated in these ablation experiment results.

## VI. RELATED WORK

In this section, we review existing approaches for vital signs tracking and explore related research in wireless-based and mmWave-based sensing. Respiration and heartbeat, essential indicators of human health, have garnered significant research attention [14]. Current approaches for monitoring these vital signs fall into two categories: contact-based and contact-free.

### A. Contact-Based Vital Signs Monitoring

Contact-based sensing technologies, such as multi-parameter monitors [5], wearable devices [33], and earphones [34], typically necessitate correct device placement for accurate operation. This often leads to discomfort and inconvenience, especially for the users who tend to be older and less technology savvy. For instance, monitors require precise electrode placement on the chest, significantly impacting the user's experience. Wearable devices and earables can only monitor vital signs when worn, which may not always be feasible due to charging requirements and long-term discomfort associated with continuous wear. Consequently, contact-based methods prove uncomfortable and unsuitable for long-term vital sign monitoring.

### B. Contact-Free Vital Signs Tracking

Among contact-free methods, researchers have explored visual approaches to monitor human vital signs. For instance, they utilize cameras to extract PPG signals based on deep learning techniques. However, these methods pose substantial privacy concerns, as few individuals are comfortable with having cameras in their bedrooms. Likewise, approaches employing microphones to capture ultrasound reflections from the human body for vital sign monitoring encounter similar privacy issues [35]. Hence, vision and sound-based methods present deployment challenges in home settings.

Wireless signal based contact-free vital signs tracking methods, typically using radio frequency (RF) signals, have received increasing attention for their privacy-preserving features. These systems utilize wireless signals reflected off the human body to detect subtle vibrations caused by breathing and heartbeat within the chest. Researchers have employed various wireless signals such as WiFi [36], UWB [8], and mmWave radar [9], [18] for monitoring human vital signs. With notable progress, respiration can now be effectively monitored. However, ensuring the robustness of heart rate and heart rate variability (HRV) tracking remains a challenge, limiting the practical application of these systems.

### C. RF-Based Sensing

Research efforts have been devoted to contact-free human activity sensing using diverse wireless signals, including WiFi [37], [38], [39], Lora [40], RFID [41], UWB [8], [42], and mmWave radar [43], [44], [45], [46], [47]. These methods infer various human activities by analyzing wireless signals reflected from the human body, enabling a wide range of applications, from fine-grained vital sign monitoring [48], [49], [50], [51] to coarse-grained gesture recognition [52], [53], tracking [54], [55], fall detection [56], and behavior recognition [57]. Among these wireless technologies, mmWave radar holds exceptional promise due to its extensive bandwidth, compact antennas, and high-frequency characteristics, making it suitable for both precise and comprehensive human activity sensing.

## VII. DISCUSSION

In this section, we discuss the limitations and potential direction of our future work.

**Bandwidth Issue:** While Robust-Vital significantly enhances the SNR by leveraging frequency diversity, making the monitoring of heart rate and HRV more robust, the algorithm concurrently reduces bandwidth, leading to decreased range resolution. However, in vital signs monitoring, range resolution is not a pivotal metric. Resolutions of 3.75 cm (corresponding to a 4G bandwidth) or 30 cm (corresponding to a 500 M bandwidth) do not impact the algorithm's performance. This is attributed to the fact that the crucial aspect of vital signs monitoring lies in the radar signal's ability to accurately capture the subtle vibrations in the human thorax, with the core metric being the SNR, unrelated to bandwidth.

**Multi-Subject Monitoring:** While Robust-Vital has achieved long-term robust monitoring of an individual's respiration rate, heart rate, and heart rate variability, the current system cannot yet be applied in situations where there are multiple people in bed. In such cases, it is challenging for mmWave radar to distinguish between them due to their close proximity. Current methods based on blind source separation can only achieve multi-person respiration rate monitoring. However, single-person vital sign monitoring has already found extensive applications in scenarios such as nursing homes and hospital beds. We consider multi-person vital sign monitoring as a future research direction.

**Early Disease Screening:** While Robust-Vital has successfully ensured stable vital sign monitoring, its full potential in early cardiopulmonary disease screening remains untapped. Currently, we've introduced a technical approach, but a definitive correlation between this data and diseases is yet to be established. Our next phase involves collaboration with hospitals to gather mmWave radar data from pertinent patients, enabling the genuine application of mmWave radar in early disease screening and proactive user health management.

## VIII. CONCLUSION

In this paper, we investigate the SNR mutation phenomenon, which has a substantial impact on the performance of mmWave-based human vital sign monitoring systems. To tackle this, we introduce a multi-point reflection model to understand the underlying causes of SNR mutation. Subsequently, we propose a frequency diversity-based algorithm designed to alleviate its effects and enhance sensing SNR. We have implemented a human heartbeat sensing system using this enhanced signal, and it has showcased superior performance.

## REFERENCES

- [1] H. Wang et al., "Human respiration detection with commodity wifi devices: Do user location and body orientation matter?", in *Proc. ACM Int. Joint Conf. Pervasive Ubiquitous Comput.*, 2016, pp. 25–36.
- [2] Y. Wang, Z. Wang, J. A. Zhang, H. Zhang, and M. Xu, "Vital sign monitoring in dynamic environment via mmWave radar and camera fusion," *IEEE Trans. Mobile Comput.*, vol. 23, no. 5, pp. 4163–4180, May 2024.
- [3] D. W. Rowe, J. Sibert, and D. Irwin, "Heart rate variability: Indicator of user state as an aid to human-computer interaction," in *Proc. SIGCHI Conf. Hum. Factors Comput. Syst.*, 1998, pp. 480–487.
- [4] A. H. Association, "Heart disease and stroke statistics," 2023. Accessed: Aug. 23, 2023. [Online]. Available: <https://professional.heart.org/en/science-news/heart-disease-and-stroke-statistics-2023-update>
- [5] P. Pandian et al., "Smart vest: Wearable multi-parameter remote physiological monitoring system," *Med. Eng. Phys.*, vol. 30, no. 4, pp. 466–477, 2008.
- [6] A. Khushhal et al., "Validity and reliability of the apple watch for measuring heart rate during exercise," *Sports Med. Int. Open*, vol. 1, no. 06, pp. E206–E211, 2017.
- [7] X. Liu et al., "rPPG-toolbox: Deep remote PPG toolbox," 2022, *arXiv:2210.00716*.
- [8] Z. Wang, B. Jin, S. Li, F. Zhang, and W. Zhang, "ECG-grained cardiac monitoring using uwb signals," *Proc. ACM Interactive, Mobile, Wearable Ubiquitous Technol.*, vol. 6, no. 4, pp. 1–25, 2023.
- [9] U. Ha, S. Assana, and F. Adib, "Contactless seismocardiography via deep learning radars," in *Proc. 26th Annu. Int. Conf. Mobile Comput. Netw.*, 2020, pp. 1–14.
- [10] T. Instruments, "Texas instruments website about mmWave radar sensors," 2023. Accessed: Aug. 06, 2023. [Online]. Available: <https://www.ti.com/sensors/mmwave-radar/overview.html>

- [11] I. T. AG, "Infineon official website about mmWave radar sensors," 2023. Accessed: Aug. 06, 2023. [Online]. Available: <https://www.infineon.com/cms/en/product/sensor/radar-sensors/>
- [12] C. S. Technology, "Calterh semiconductor technology's official website," 2017. Accessed: Aug. 12 2023. <https://www.calterah.com/>
- [13] W. Zhang, G. Li, Z. Wang, and H. Wu, "Non-contact monitoring of human heartbeat signals using mm-Wave frequency-modulated continuous-wave radar under low signal-to-noise ratio conditions," *IET Radar, Sonar Navigation*, vol. 16, no. 3, pp. 456–469, 2022.
- [14] F. Adib, H. Mao, Z. Kabelac, D. Katabi, and R. C. Miller, "Smart homes that monitor breathing and heart rate," in *Proc. 33rd Annu. ACM Conf. Hum. Factors Comput. Syst.*, 2015, pp. 837–846.
- [15] T. Zheng, Z. Chen, C. Cai, J. Luo, and X. Zhang, "V2iFi: In-vehicle vital sign monitoring via compact RF sensing," *Proc. ACM Interactive, Mobile, Wearable Ubiquitous Technol.*, vol. 4, no. 2, pp. 1–27, 2020.
- [16] X. Xu et al., "mmECG: Monitoring human cardiac cycle in driving environments leveraging millimeter wave," in *Proc. IEEE Conf. Comput. Commun.*, 2022, pp. 90–99.
- [17] G. Ramachandran and M. Singh, "Three-dimensional reconstruction of cardiac displacement patterns on the chest wall during the P, QRS and T-segments of the ECG by laser speckle interferometry," *Med. Biol. Eng. Comput.*, vol. 27, pp. 525–530, 1989.
- [18] A. Ahmad, J. C. Roh, D. Wang, and A. Dubey, "Vital signs monitoring of multiple people using a FMCW millimeter-wave sensor," in *Proc. IEEE Radar Conf.*, 2018, pp. 1450–1455.
- [19] P. Zheng, C. Zheng, X. Li, H. Chen, A. Wang, and Y. Luo, "Second harmonic weighted reconstruction for non-contact monitoring heart rate," *IEEE Sensors J.*, vol. 22, no. 6, pp. 5815–5823, Mar. 2022.
- [20] H. Xu, M. P. Ebrahim, K. Hasan, F. Heydari, P. Howley, and M. R. Yuce, "Accurate heart rate and respiration rate detection based on a higher-order harmonics peak selection method using radar non-contact sensors," *Sensors*, vol. 22, no. 1, 2021, Art. no. 83.
- [21] S. Ji, H. Wen, J. Wu, Z. Zhang, and K. Zhao, "Systematic heartbeat monitoring using a FMCW mm-Wave radar," in *Proc. IEEE Int. Conf. Consum. Electron. Comput. Eng.*, 2021, pp. 714–718.
- [22] C. Li, V. M. Lubecke, O. Boric-Lubecke, and J. Lin, "A review on recent advances in doppler radar sensors for noncontact healthcare monitoring," *IEEE Trans. Microw. Theory Techn.*, vol. 61, no. 5, pp. 2046–2060, May 2013.
- [23] M. A. Richards, *Fundamentals of Radar Signal Processing*. New York, NY, USA: McGraw-Hill Education, 2022.
- [24] A. G. Stove, "Linear FMCW radar techniques," *IEE Proc. F Radar Signal Process.*, vol. 139, no. 5, pp. 343–350, 1992.
- [25] C. Jiang, J. Guo, Y. He, M. Jin, S. Li, and Y. Liu, "mmVib: Micrometer-level vibration measurement with mmWave radar," in *Proc. 26th Annu. Int. Conf. Mobile Comput. Netw.*, 2020, pp. 1–13.
- [26] Y. Li et al., "Diversense: Maximizing wi-fi sensing range leveraging signal diversity," *Proc. ACM Interactive, Mobile, Wearable Ubiquitous Technol.*, vol. 6, no. 2, pp. 1–28, 2022.
- [27] F. Shaffer, R. McCraty, and C. L. Zerr, "A healthy heart is not a metronome: An integrative review of the heart's anatomy and heart rate variability," *Front. Psychol.*, vol. 5, 2014, Art. no. 1040.
- [28] T.-Y. J. Kao and J. Lin, "Vital sign detection using 60-GHz doppler radar system," in *Proc. IEEE Int. Wirel. Symp.*, 2013, pp. 1–4.
- [29] S. Dong, Y. Li, J. Lu, Z. Zhang, C. Gu, and J. Mao, "Accurate detection of doppler cardiograms with a parameterized respiratory filter technique using a k-band radar sensor," *IEEE Trans. Microw. Theory Techn.*, vol. 71, no. 1, pp. 71–82, Jan. 2023.
- [30] Y. Xiong, Z. Peng, C. Gu, S. Li, D. Wang, and W. Zhang, "Differential enhancement method for robust and accurate heart rate monitoring via microwave vital sign sensing," *IEEE Trans. Instrum. Meas.*, vol. 69, no. 9, pp. 7108–7118, Sep. 2020.
- [31] W. Liu, S. Cao, and Y. Chen, "Applications of variational mode decomposition in seismic time-frequency analysis," *Geophysics*, vol. 81, no. 5, pp. V365–V378, 2016.
- [32] K. J. Wu and C.-L. Yang, "Heart rate extraction with VMD algorithm in non-stationary clutter environment based on FMCW radar systems," in *Proc. IEEE Int. Symp. Radio-Freq. Integration Technol.*, 2021, pp. 1–3.
- [33] A. Tavakoli, M. Boukhechba, and A. Heydarian, "Leveraging ubiquitous computing for empathetic routing: A naturalistic data-driven approach," in *Proc. CHI Conf. Hum. Factors Comput. Syst.*, 2021, pp. 1–6.
- [34] T. Ahmed, M. M. Rahman, E. Nemati, M. Y. Ahmed, J. Kuang, and A. J. Gao, "Remote breathing rate tracking in stationary position using the motion and acoustic sensors of earables," in *Proc. CHI Conf. Hum. Factors Comput. Syst.*, 2023, pp. 1–22.
- [35] L. Wang et al., "LoEar: Push the range limit of acoustic sensing for vital sign monitoring," *Proc. ACM Interactive, Mobile, Wearable Ubiquitous Technol.*, vol. 6, no. 3, pp. 1–24, 2022.
- [36] K. Ali, M. Alloulah, F. Kawzar, and A. X. Liu, "On goodness of WiFi based monitoring of sleep vital signs in the wild," *IEEE Trans. Mobile Comput.*, vol. 22, no. 1, pp. 341–355, Jan. 2023.
- [37] Y. Wang, K. Wu, and L. M. Ni, "WiFall: Device-free fall detection by wireless networks," *IEEE Trans. Mobile Comput.*, vol. 16, no. 2, pp. 581–594, Feb. 2017.
- [38] X. Wang et al., "Understanding the diffraction model in static multipath-rich environments for WiFi sensing system design," *IEEE Trans. Mobile Comput.*, early access, Mar. 28, 2024, doi: [10.1109/TMC.2024.337708](https://doi.org/10.1109/TMC.2024.337708).
- [39] Z. Yao, X. Wang, K. Niu, R. Zheng, J. Wang, and D. Zhang, "Wiprofile: Unlocking diffraction effects for sub-centimeter target profiling using commodity wifi devices," in *Proc. 30th Annu. Int. Conf. Mobile Comput. Netw.*, 2024, pp. 185–199.
- [40] Z. Chang, F. Zhang, J. Xiong, J. Ma, B. Jin, and D. Zhang, "Sensor-free soil moisture sensing using LoRa signals," *Proc. ACM Interactive, Mobile, Wearable Ubiquitous Technol.*, vol. 6, no. 2, pp. 1–27, 2022.
- [41] X. Liu et al., "Accurate localization of tagged objects using mobile RFID-augmented robots," *IEEE Trans. Mobile Comput.*, vol. 20, no. 4, pp. 1273–1284, Apr. 2021.
- [42] P. Wang et al., "SlpRoF: Improving the temporal coverage and robustness of RF-based vital sign monitoring during sleep," *IEEE Trans. Mobile Comput.*, vol. 23, no. 7, pp. 7848–7864, Jul. 2024.
- [43] D. Zhang et al., "Lt-fall: The design and implementation of a life-threatening fall detection and alarming system," *Proc. ACM Interactive, Mobile, Wearable Ubiquitous Technol.*, vol. 7, no. 1, pp. 1–24, 2023.
- [44] D. Zhang et al., "Local: An automatic location attribute calibration approach for large-scale deployment of mmwave-based sensing systems," *Proc. ACM Interactive, Mobile, Wearable Ubiquitous Technol.*, vol. 7, no. 4, pp. 1–27, 2024.
- [45] X. Zhang, D. Zhang, Y. Xie, D. Wu, Y. Li, and D. Zhang, "Waffle: A waterproof mmwave-based human sensing system inside bathrooms with running water," *Proc. ACM Interactive, Mobile, Wearable Ubiquitous Technol.*, vol. 7, no. 4, pp. 1–29, 2024.
- [46] J. Guo et al., "Measuring micrometer-level vibrations with mmWave radar," *IEEE Trans. Mobile Comput.*, vol. 22, no. 4, pp. 2248–2261, Apr. 2023.
- [47] J. Chen, D. Zhang, Z. Wu, F. Zhou, Q. Sun, and Y. Chen, "Contactless electrocardiogram monitoring with millimeter wave radar," *IEEE Trans. Mobile Comput.*, vol. 23, no. 1, pp. 270–285, Jan. 2024.
- [48] J. Liu, Y. Zeng, T. Gu, L. Wang, and D. Zhang, "WiPhone: Smartphone-based respiration monitoring using ambient reflected WiFi signals," *Proc. ACM Interactive, Mobile, Wearable Ubiquitous Technol.*, vol. 5, no. 1, pp. 1–19, 2021.
- [49] F. Zhang, J. Xiong, Z. Chang, J. Ma, and D. Zhang, "Mobi2Sense: Empowering wireless sensing with mobility," in *Proc. 28th Annu. Int. Conf. Mobile Comput. Netw.*, 2022, pp. 268–281.
- [50] Z. Chang, F. Zhang, J. Xiong, W. Chen, and D. Zhang, "MSense: Boosting wireless sensing capability under motion interference," in *Proc. 30th Annu. Int. Conf. Mobile Comput. Netw.*, 2024, pp. 108–123.
- [51] F. Zhang et al., "Embracing consumer-level UWB-equipped devices for fine-grained wireless sensing," *Proc. ACM Interactive, Mobile, Wearable Ubiquitous Technol.*, vol. 6, no. 4, pp. 1–27, 2023.
- [52] Y. Li et al., "Towards domain-independent and real-time gesture recognition using mmWave signal," *IEEE Trans. Mobile Comput.*, vol. 22, no. 12, pp. 7355–7369, Dec. 2023.
- [53] R. Gao et al., "Towards robust gesture recognition by characterizing the sensing quality of WiFi signals," *Proc. ACM Interactive, Mobile, Wearable Ubiquitous Technol.*, vol. 6, no. 1, pp. 1–26, 2022.
- [54] X. Li et al., "Indotrack: Device-free indoor human tracking with commodity Wi-Fi," *Proc. ACM Interactive, Mobile, Wearable Ubiquitous Technol.*, vol. 1, no. 3, pp. 1–22, 2017.
- [55] W. Li et al., "WiFi-CSI difference paradigm: Achieving efficient doppler speed estimation for passive tracking," *Proc. ACM Interactive, Mobile, Wearable Ubiquitous Technol.*, vol. 8, no. 2, pp. 1–29, 2024.
- [56] S. Chen, W. Yang, Y. Xu, Y. Geng, B. Xin, and L. Huang, "AFall: Wi-Fi-based device-free fall detection system using spatial angle of arrival," *IEEE Trans. Mobile Comput.*, vol. 22, no. 8, pp. 4471–4484, Aug. 2023.
- [57] X. Wang, T. Liu, C. Feng, D. Fang, and X. Chen, "RF-CM: Cross-modal framework for RF-enabled few-shot human activity recognition," *Proc. ACM Interactive, Mobile, Wearable Ubiquitous Technol.*, vol. 7, no. 1, pp. 1–28, 2023.



**Duo Zhang** received the bachelor's degree in computer science and technology from the School of Computer Science, Northwestern Polytechnical University, Xi'an, China, in 2021. He is currently working toward the PhD degree in computer science with the School of Computer Science, Peking University, Beijing, China. His research interests include ubiquitous computing, mobile computing, and wireless sensing.



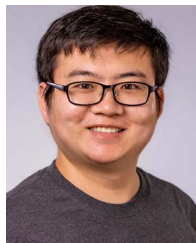
**Fusang Zhang** received the MS and PhD degrees in computer science from the Institute of Software, Chinese Academy of Sciences, Beijing, China, in 2013 and 2017, respectively. He is currently an associate professor with the Institute of Software, Chinese Academy of Sciences. His current research interests include mobile and pervasive computing, wireless contactless sensing and quantum sensing.



**Xusheng Zhang** received the bachelor's degree in computer science and technology from the School of Computer Science, Chongqing University, Chongqing, China, in 2021. He is currently working toward the PhD degree in computer science with the School of Computer Science, Peking University, Beijing, China. His research interests include ubiquitous computing, mobile computing, and wireless sensing.



**Hongliu Yang** received the bachelor's degree in information engineering from School of Information and Communication Engineering, Beijing University of Posts and Telecommunications, Beijing, China in 2023. He is currently working toward the PhD degree with the School of Computer Science, Peking University. His current research interests include ubiquitous computing, mobile computing, and wireless sensing.



**Yaxiong Xie** received the PhD degree from Nanyang Technological University in Singapore. He is an assistant professor with the Department of Computer Science and Engineering at the University at Buffalo, SUNY. Before joining UB, he was a postdoctoral researcher with Princeton University. His research broadly focuses on mobile sensing and mobile networks, with specific emphasis on two areas: applying mobile sensing for smart health applications and building next-generation mobile networks to support diverse applications such as video streaming, video conferencing, and video analytics. His recent research has been published in top conferences, including SIGCOMM, MobiCom, NSDI, UbiComp, SenSys, and SigMetrics.



**Daqing Zhang** (Fellow, IEEE) received the PhD degree from the University of Rome "La Sapienza," Roma, Italy, in 1996. He is currently a chair professor with the Key Laboratory of High Confidence Software Technologies (Ministry of Education), School of Computer Science, Peking University, China, and Telecom SudParis, IP Paris, France. His research interests include context-aware computing, urban computing, mobile computing, Big Data analytics, pervasive elderly care, etc. He has authored more than 300 technical papers in leading conferences and journals. He was the general or program chair for more than 17 international conferences, giving keynote talks at more than 20 international conferences. He is the associate editor for *IEEE Pervasive Computing*, *ACM Transactions on Intelligent Systems and Technology*, and *Proceeding of ACM on Interactive, Mobile, Wearable and Ubiquitous Technologies*. He is the winner of TenYears CoMoRea Impact Paper Award at IEEE PerCom 2013 and TenYears Most Influential Paper Award at IEEE UIC 2019, Honorable Mention Award at ACM UbiComp 2015 and 2016, and Distinguished Paper Award at ACM UbiComp 2021.